

Article

Engineering Band Structure of SnO₂ Nanoparticles via Coupling with g-C₃N₄ Nanosheet for the Detection of Ethanolamine

Jiuyu Li ¹, Kerui Xie ¹, Yating Wang ¹, Ruihua Zhao ¹, Yangyang Shang ¹ and Jianping Du ^{1,2,3,*} 

¹ College of Chemical and Engineering Technology, Taiyuan University of Technology, 79 Yingze West Street, Taiyuan 030024, China

² College of Chemistry, Taiyuan University of Technology, 79 Yingze West Street, Taiyuan 030024, China

³ Key Laboratory of Gas Energy Efficient and Clean Utilization, Taiyuan University of Technology, Taiyuan 030024, China

* Correspondence: dujp518@163.com

Abstract: Volatile organoamines are important industrial raw materials and chemicals. Long-term exposure to amines could be harmful to human health and even cause serious pollution. In this study, SnO₂ decorated g-C₃N₄ material was fabricated and used as a sensor material for the detection of ethanolamine (EA). The structures, morphology, surface chemical states, and band structure were characterized, and gas sensing was studied. The results showed that SnO₂ nanoparticles were dispersed on g-C₃N₄, and band structure was dependent on g-C₃N₄ doping. Notably, the interface heterojunction was conducive to electron transferring and O₂ molecule adsorption; the formed reactive oxygen species enhanced the reaction between oxygen and EA, thus leading to high sensitivity to EA. This composite exhibited a high response that was 2.6 times higher than that of pure SnO₂, and the detection limit reached 294 ppb. A g-C₃N₄/SnO₂-based sensor displayed a high selectivity to EA with a fast response time (1 s) and recovery time (20 s) at low operating temperatures. In particular, this sensor exhibited a linear relationship between the response and concentration, which is required for quantitative analysis.

Keywords: g-C₃N₄/SnO₂; heterojunction; band structure; ethanolamine; sensors



Citation: Li, J.; Xie, K.; Wang, Y.; Zhao, R.; Shang, Y.; Du, J.

Engineering Band Structure of SnO₂ Nanoparticles via Coupling with g-C₃N₄ Nanosheet for the Detection of Ethanolamine. *Chemosensors* **2023**, *11*, 296. <https://doi.org/10.3390/chemosensors11050296>

Academic Editor: Simonetta Capone

Received: 28 March 2023

Revised: 26 April 2023

Accepted: 10 May 2023

Published: 16 May 2023



Copyright: © 2023 by the authors. Licensee MDPI, Basel, Switzerland. This article is an open access article distributed under the terms and conditions of the Creative Commons Attribution (CC BY) license (<https://creativecommons.org/licenses/by/4.0/>).

1. Introduction

Volatile organic amine compounds (VOACs) have a wide range of sources [1]. Natural sources mainly include animal excrement, animal and plant remains, and microbial products; non-natural sources mainly include chemical production, industrial waste discharge, and domestic waste. The harm inflicted on living organisms and the ecological environment by VOACs should not be underestimated. The excessive presence of VOACs will cause biological poisoning and environmental deterioration [2]. In China, the emissions from non-natural sources are much higher than those from natural sources [3]. It is not enough to rely on the self-regulation of the ecosystem. Therefore, it is necessary to deal with these harmful compounds artificially. Strengthening the monitoring of VOACs such as triethylamine (TEA) and ethanolamine (EA) is an important means to control their emissions and reduce their harm, so suitable detection methods and detection materials are particularly needed.

VOCs are usually detected via spectrometry, chromatography, etc., which have the advantages of low error rates and strong stability. However, their operation is complicated; they usually need to be used in combination with other instruments, and these factors restrict their portable applications. Therefore, it is necessary to develop sensing material to quickly detect VOCs on a large scale. In this regard, semiconductor metal oxide materials, due to their simple preparation and low cost, are recognized as materials with applications

in chemical sensors [4–8]. Our previous research reported strategies for the application of ZnO and SnO₂ via non-metal and metal doping, and we found that different, modified oxides can respond to different amines, such as S-ZnO for EA [9] and Cr-SnO₂ for TEA [10]. Another case is CuO/SnO₂: the heterojunction between the interface of CuO and SnO₂ cause this composite to exhibit a high response to TEA [11]. For comparison, SnO₂ is also a common sensing material [12–15]. For example, Zhang et al. prepared nanostructural SnO₂ for ethanol detection and improved its performance [16]. Ma et al. prepared mesoporous SnO₂ for the fast detection of formaldehyde [17]. Din et al. developed NiO/SnO₂ heterojunction material to detect ethanol, and it exhibited a high performance [18]. Dai et al. prepared rod-like Au-modified ZnO nanoflowers for EA detection [19]. However, doped and oxide-modified SnO₂ is only efficient in the identification of TEA and other VOCs. In order to improve its response to EA, we chose to disperse SnO₂ on a matrix and construct a heterojunction by introducing non-metallic materials to this material.

Graphitic carbon nitride (g-C₃N₄), which possesses a two-dimensional structure and is composed of carbon and nitrogen atoms, is a promising sensitization material [20]. It is an n-type semiconductor material with many advantages, such as a high specific surface area, excellent catalytic properties, remarkable two-dimensional material properties, and a gas adsorption ability [21], so it has attracted the attention of many researchers. g-C₃N₄ has been used in photocatalysis [22,23], energy storage [24], gas sensing [25], and optoelectronic devices [26]. Because of its distinctive two-dimensional structure, it can be used to improve the gas sensitivity of semiconductor metal oxides for applications in gas sensors.

g-C₃N₄ can form heterogeneous structures with semiconductor metal oxides, which can not only cause metal oxide nanoparticles to have good dispersibility but also optimize their gas sensitivity. Cao et al. [27] synthesized a SnO₂ compound material with two-dimensional g-C₃N₄ nanosheets via a hydrothermal route, and the compound demonstrated a high sensitivity to ethanol gas. The sensitivity to 500 ppm ethanol gas was 240 at 300 °C. Lu et al. [28] prepared a 2D/2D ZnO/g-C₃N₄ heterojunction material, and the results showed excellent NO₂ sensing performance and a response to 7 ppm NO₂ that reached 44.8. Niu et al. prepared mesoporous Co₃O₄ nanowires modified with g-C₃N₄ nanosheets, and this composite displayed a high level of response to toluene gas [29]. The high surface area and great electronic structure of two-dimensional g-C₃N₄ are beneficial to improving the gas sensitivity of semiconductors. These composites have enhanced response rates and selectivity compared to pure metal oxides.

In this work, SnO₂-decorated g-C₃N₄ materials were synthesized and characterized, and the band structure was regulated by changing g-C₃N₄. Gas-sensing performance was studied based on the response to volatile organic compounds.

2. Experimental

2.1. Chemicals and Reagents

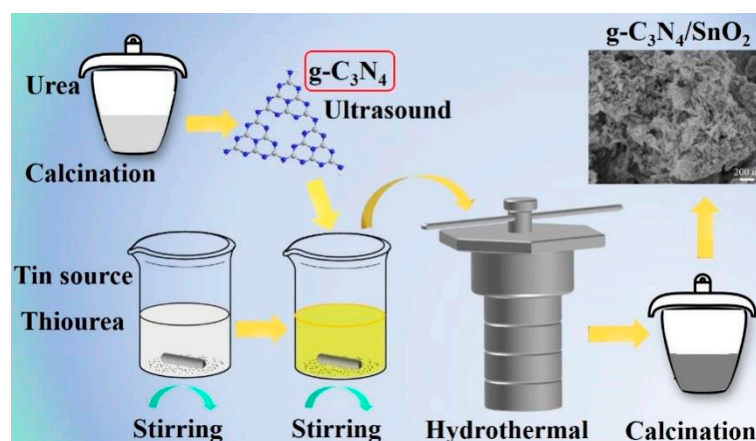
All reagents were analytical grade and were not further purified before use. Urea was purchased from Tianjin Cameo Chemical Reagent Co., Ltd., Tianjin, China. Stannous chloride was purchased from Tianjin Guangfu Technology Development Co., Ltd., Tianjin, China. Thiourea was purchased from Tianjin Kaitong Chemical Reagent Co. Ltd., Tianjin, China. EA was purchased from Tianjin Fuchen Chemical Reagent Co. Ltd., Tianjin, China.

2.2. Preparation of g-C₃N₄

Graphitic carbon nitride (g-C₃N₄) was directly synthesized by pyrolysis urea in a muffle furnace. First, 20 g urea was put into an alumina crucible with a cover, then kept at 550 °C for 4 h (heating rate $v = 10$ °C/min). The light yellow g-C₃N₄ sample was collected. A certain amount of light yellow g-C₃N₄ powder was ultrasonically treated in deionized water for 60 min and then dried.

2.3. Synthesis of SnO_2 and $\text{g-C}_3\text{N}_4/\text{SnO}_2$ Materials

The procedure of material synthesis is shown in Scheme 1. In a typical synthesis of $\text{g-C}_3\text{N}_4/\text{SnO}_2$ -5, 16 mmol stannous chloride and 16 mmol thiourea were dissolved in 120 mL deionized water and stirred for 50 h, resulting in a solution labeled A. The theoretical content of 5 wt% $\text{g-C}_3\text{N}_4$ was stirred and mixed with 30 mL A suspension for 30 min and then kept at 140°C for 8 h. The $\text{g-C}_3\text{N}_4/\text{SnO}_2$ -5 sample was obtained via centrifugation with deionized water and dried, followed by heat treatment for 2 h at 550°C in air. According to the same procedure, pure SnO_2 and SnO_2 hybrid synthesized by changing $\text{g-C}_3\text{N}_4$ amount, which were labeled as $\text{g-C}_3\text{N}_4/\text{SnO}_2$ -x (x is the theoretical mass fraction of $\text{g-C}_3\text{N}_4$ to SnO_2 , i.e., 2.5% and 10%).



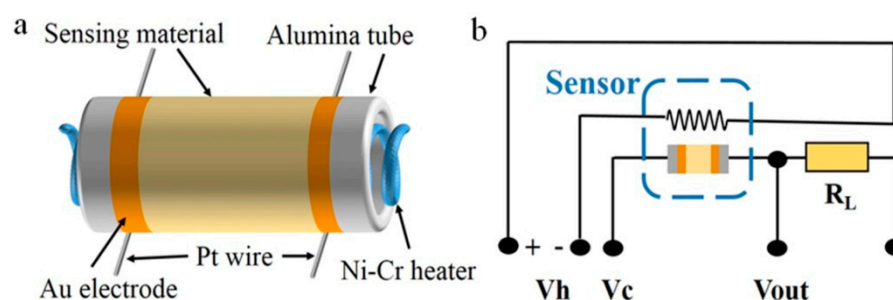
Scheme 1. Synthetic procedure of $\text{g-C}_3\text{N}_4$ decorated SnO_2 materials.

2.4. Characterization of $\text{g-C}_3\text{N}_4/\text{SnO}_2$ Materials

The crystal structures of as-synthesized $\text{g-C}_3\text{N}_4/\text{SnO}_2$ materials were analyzed via XRD (Shimadzu, Tokyo, Japan, XRD-6000, with high-intensity $\text{Cu K}\alpha$ radiation, $\lambda = 0.15418$ nm). The morphology and microstructure were observed via SEM (Hitachi SU8010, Hitachi, Japan) and TEM (JEOL, JEM-2100F, Tokyo, Japan) at the accelerating voltage of 5 kV and 200 kV, respectively. The specific surface areas of the materials were recorded via the Bronner–Emmett–Teller (BET) method, and the pore structures were analyzed using N_2 adsorption–desorption technique (Micromeritics Tristar II 3020, Atlanta, GA, USA).

2.5. Fabrication of Sensors and VOCs Detection

The gas sensors for the tests were fabricated as follows. Briefly, the SnO_2 -based materials are dispersed by mixing the as-synthesized SnO_2 or $\text{g-C}_3\text{N}_4/\text{SnO}_2$ powder with ethanol. A few drops of dispersion were coated thinly and evenly onto the surface of alumina ceramic tube with Au electrodes, Pt wires, and Ni-Cr wire as heater (Scheme 2a). Ceramic tubes coated with SnO_2 -based materials were dried at 80°C for 1h and then heated at 300°C for 2 h. Finally, the element should be welded on the pedestal and then inserted in the test circuit (Scheme 2b).



Scheme 2. The construction of gas sensor (a) and electric circuit of test device (b).

The gas sensing properties were measured using WS-30A static test system (Winsen Electronics Co. Ltd., Zhengzhou, China). The sensitivity (S) of sensor is defined as R_a/R_g , where R_a and R_g denote the resistance in air and target gas, respectively. The environment's humidity is about 35%.

3. Results and Discussion

Figure 1a illustrates the synthetic route of SnO₂ nanoparticles anchored on the g-C₃N₄ (g-C₃N₄/SnO₂) by simple hydrolysis at room temperature, hydrothermal, and heat treatment. Thiourea was used as the accelerant and stabilizer, and the yellow precursor was obtained by hydrolysis, dehydration, and partial oxidation of stannous ion. This is a slow process in which only a small amount of Sn²⁺ is oxidized to tin dioxide. In the stirring process, thioureas (CH₄N₂S), which produce amino (–NH₂), imino(–NH), and mercaptan (–SH), react with HCl generated via hydrolysis of tin tetrachloride (SnCl₄), which accelerates the continuous hydrolysis process. Moreover, the coupling of Sn⁴⁺ with sulfhydryl groups plays a stabilizing role, contributing to the formation of stable nanoscale particles. During the hydrothermal process, g-C₃N₄ is agglomerated on the surface, forming a sheet structure of g-C₃N₄ coated with tin dioxide precursor nanoparticles. Finally, the g-C₃N₄ composite coated with SnO₂ nanoparticles was prepared via drying and calcination.

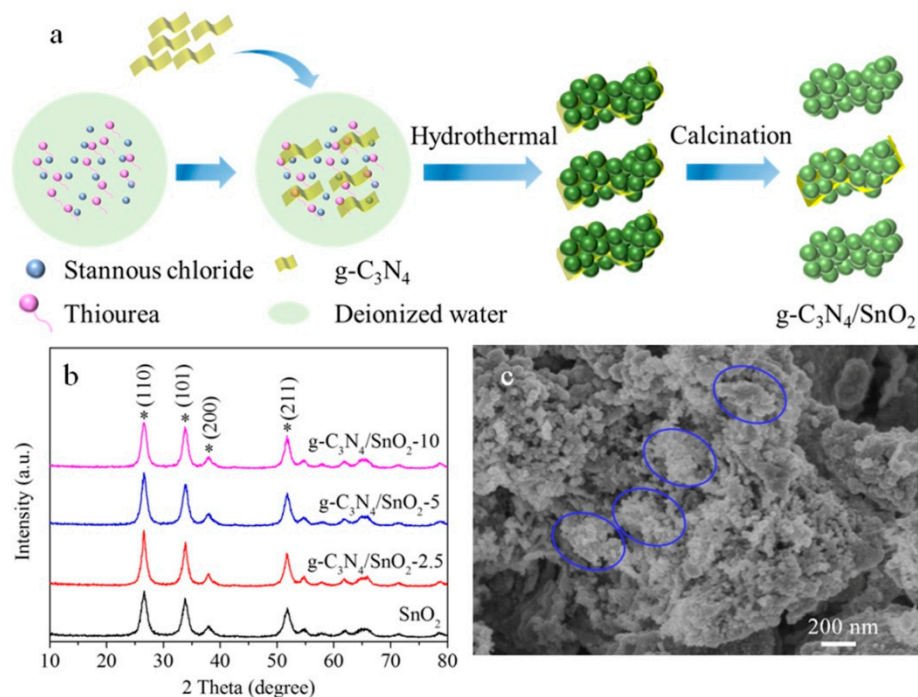


Figure 1. (a) Schematic diagram of the formation process; (b) XRD patterns of as-synthesized g-C₃N₄/SnO₂ (* denotes SnO₂ characteristic peaks); (c) SEM image of g-C₃N₄/SnO₂-5 material.

The phase structure and crystal structure were characterized via XRD. Figure S1 shows (100) and (002) planes corresponding to g-C₃N₄ (JCPDS, No. 87-1526) at 13.0° and 27.6°, respectively. Figure 1b shows the XRD patterns of the pure SnO₂ nanoparticles and g-C₃N₄/SnO₂ composites. The positions of 26.6°, 33.9°, 37.9°, and 51.8°, where the diffraction peaks are located, corresponding to (110), (101), (200), and (211) planes of the tetragonal rutile structure SnO₂ (JCPDS, No. 41-1445), respectively. However, no other peaks of impurity, including g-C₃N₄ diffraction peaks, were detected in the XRD patterns, which may be due to the trace amounts of g-C₃N₄ in the g-C₃N₄/SnO₂ composite materials, which did not reach the detection limit of the XRD. It is also possible that the diffraction peak of g-C₃N₄ near 27.6° and that of SnO₂ at 26.6° overlaps. There is no obvious diffraction peak shift in the diffraction pattern, indicating that g-C₃N₄ and SnO₂ do not exist independently, which means that n-n heterojunctions form on the contact interface between

the two materials. Figure 1c shows the morphology of the g-C₃N₄/SnO₂-5 composite. SnO₂ nanoparticles are dispersed on the nanosheets of g-C₃N₄ and form a supported particle group (shown with a blue oval). The SEM images of g-C₃N₄, SnO₂, and other g-C₃N₄/SnO₂ show layer, nanoparticles aggregation, and nanosheets-supported particle group (Figure S2).

In order to analyze the chemical composition and state of g-C₃N₄/SnO₂-5 material, XPS characterization was performed. Figure S3 shows the full XPS spectrum of g-C₃N₄/SnO₂-5 material, in which the peaks are related to C, N, O, and Sn. It indicates the successful synthesis of g-C₃N₄/SnO₂ composite material, which indirectly proves the existence of heterojunction between g-C₃N₄ and SnO₂.

Figure 2a shows the high-resolution spectrum of C 1s, and the binding energies of 284.5, 285.1, 286.2, and 286.9 eV belong to the C-C bond of sp², C-N, C-NH₂, and C=NH in the triazine ring, respectively [30]. Figure 2b shows the spectrum of N 1s, and the binding energies of 399.7, 401.7, 402.00 eV and 402.65 eV belong to sp² hybrid nitrogen (C-N=C), tertiary nitrogen (N-(C)₃), N-O and C-N-H structure, respectively [31]. It indicates the existence of g-C₃N₄ in the g-C₃N₄/SnO₂-5 composite. Figure 2c is the spectrum of O 1s, and the peaks appear at 530.95 and 531.8 eV. The peak at 530.95 eV is attributed to the lattice oxygen of SnO₂, and the peak at 531.8 eV is attributed to defective oxygen. In Figure 2d, the peaks of 495.5 eV and 487.15 eV correspond to Sn 3d_{3/2} and Sn 3d_{5/2}, indicating that Sn exists in the form of Sn⁴⁺. The results show that the material is composed of g-C₃N₄ and SnO₂.

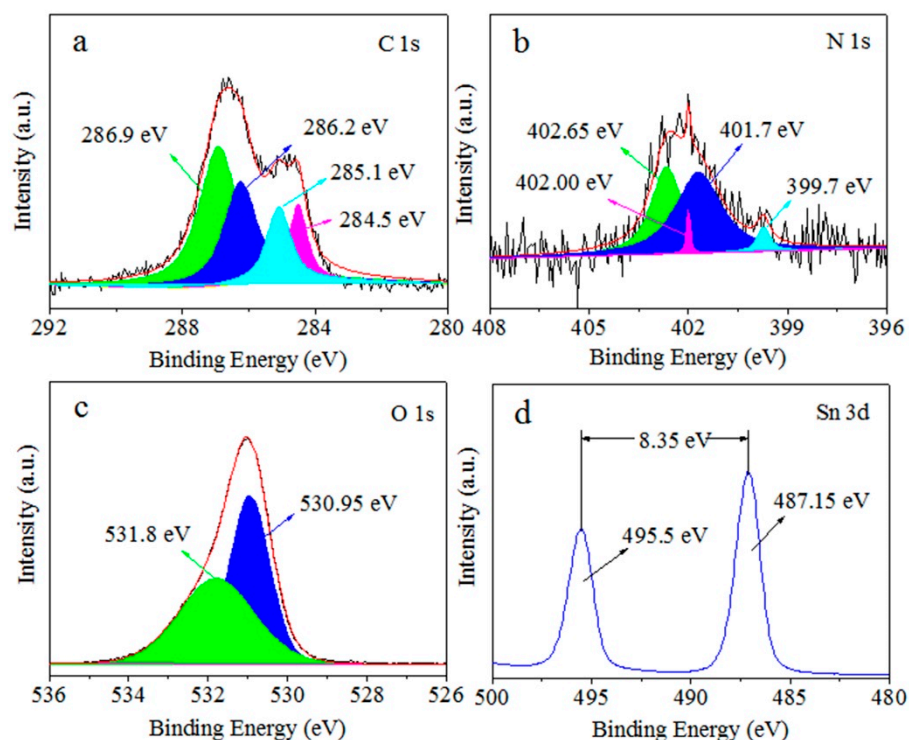


Figure 2. XPS spectra of the C 1s (a), N 1s (b), O 1s (c), and Sn 3d (d) of as-synthesized g-C₃N₄/SnO₂-5 nanomaterial.

Figure 3a shows that SnO₂ and g-C₃N₄/SnO₂-5 materials possess characteristics of type IV isotherms, and the specific surface areas of SnO₂ and g-C₃N₄/SnO₂-5 are 24.5 and 25.7 m² g⁻¹, respectively. When the relative pressure P/P₀ is between 0.4 and 1.0, the adsorption capacity rises rapidly, showing a H3-type hysteresis loop, indicating that a narrow-slit aggregate structure is formed between g-C₃N₄ and SnO₂ nanoparticles, and there are abundant mesoporous structures. Figure 3b shows the pore size distribution of SnO₂ and g-C₃N₄/SnO₂-5. It can be seen from the figure that both materials have smaller

pore size distributions, and the average pore sizes of SnO₂ and g-C₃N₄/SnO₂-5 are 8.2 nm and 10.8 nm, respectively. The increased specific surface area is beneficial to improve the gas sensing property.

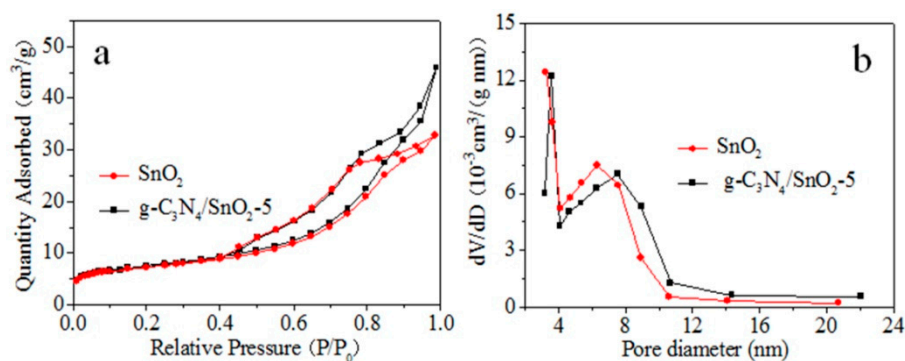


Figure 3. N₂ adsorption–desorption isotherms (a) and pore size distribution (b) of as-synthesized g-C₃N₄/SnO₂-5.

The gas-sensing properties of these materials in the atmosphere were investigated. The working temperature has a great influence on the reaction kinetics of gas molecules and oxygen on the surface of the material, and it also has an effect on the gas-sensing behavior of the material. The optimal working temperature of SnO₂ and g-C₃N₄/SnO₂ materials for detecting ethanolamine (EA) was explored. Figure 4a shows the response of the sensor to 100 ppm EA gas in the test range of 200–280 °C. The optimal operating temperature is 240 °C for the four samples obtained by changing the g-C₃N₄ content. The response to EA increases with increasing temperature when the temperature is less than 240 °C. The possible reason for this is that when the optimal working temperature is lower than 240 °C, the activity of adsorbed oxygen on the surface of SnO₂-based materials gradually increases with the increase in temperature, and the sensitivity to EA shows an upward trend. When the optimal working temperature is higher than 240 °C, the oxygen molecules, which are adsorbed on the surface of SnO₂-based materials, are rapidly desorbed before reaction with EA molecules as temperature increases, resulting in a decrease in the sensitivity to EA. It can also be seen that the sensitivity to EA increases first and then decreases with the increase in g-C₃N₄ content in SnO₂-based materials at the optimum working temperature. The g-C₃N₄/SnO₂-5 shows the best gas sensitivity. The responses of pure SnO₂, g-C₃N₄/SnO₂-2.5, g-C₃N₄/SnO₂-5, and g-C₃N₄/SnO₂-10 to 100 ppm EA are 16.5, 18.7, 23.3, and 22, respectively. The optimal amount of g-C₃N₄ doped in SnO₂ is conducive to better dispersion of the composite. The formation of heterojunctions and the increase in defects, which are between the 2D sheet g-C₃N₄ and SnO₂ nanoparticles, provide more active sites for gas adsorption and reaction, and active sites improve the gas sensitivity. However, when the content of g-C₃N₄ in the composite exceeds a certain threshold (5 wt%), g-C₃N₄ nanosheets can be connected to form a micro-bridge on the surface. The micro-bridge may result in the reduction of the resistance of the g-C₃N₄/SnO₂ composite, finally leading to a decrease in the performance of gas sensing.

Selectivity is also one of the important parameters to measure the gas-sensing performance of materials. At the optimum operating temperature of 240 °C, the sensing properties of SnO₂-based materials with different g-C₃N₄ contents to 100 ppm of volatile organic compounds are tested. The results indicate good selectivity to EA (Figure 4b), which may be due to the fact that the bond energy of the C-N bond in the EA molecule is 307 kJ mol⁻¹, indicating EA has strong reducibility compared with other volatile organic compounds. Therefore, as-prepared material exhibits better selectivity to EA. In addition, selectivity is dependent on the type of oxides and structure of composites. This is the reason that ZnO/g-C₃N₄ has no response to EA and only to DMA [21].

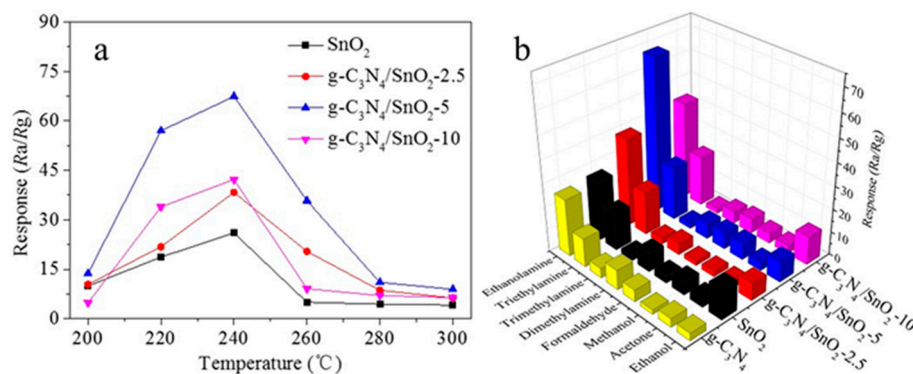


Figure 4. (a) The response to 100 ppm EA at different temperatures; (b) selectivity to EA on exposure to various volatile gases.

Figure 5a shows the transient response–recovery characteristics of SnO₂ and g-C₃N₄/SnO₂ to EA in the concentration range of 1 to 100 ppm at 240 °C. The results show that materials have a fast response and recovery ability for EA detection in a wide concentration range, and the response increases with increasing concentration. Notably, these materials exhibit an obvious response to 1–10 ppm of low-concentration EA (Figure 5b). Figure 6a displays a good linear relationship between response and concentration of EA. The detection limit of the g-C₃N₄/SnO₂-5 sensor to EA is 294 ppb. To explore the stability of the g-C₃N₄/SnO₂-5 sensor, the responses to low-concentration EA were recorded within nine days (Figure 6b), and the response value to 100 ppm EA at interval of 2 days reaches around 50 after 5 days, indicating g-C₃N₄/SnO₂-5 sensor has better stability to EA.

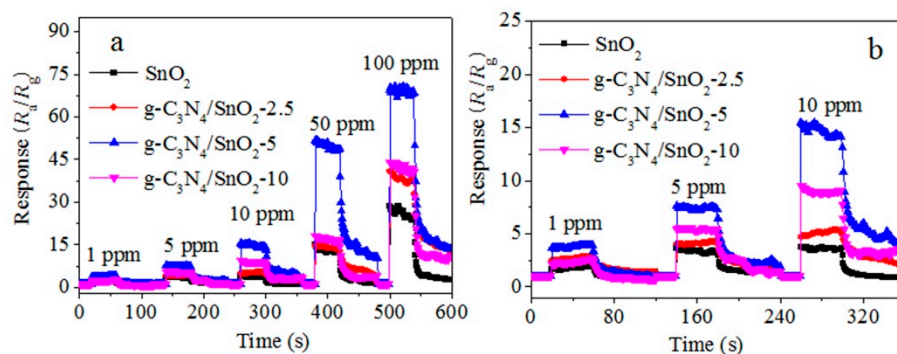


Figure 5. Transient response–recovery profiles of composite material at 240 °C after exposure to (a) different concentration EA and (b) low concentration (1–5 ppm) EA.

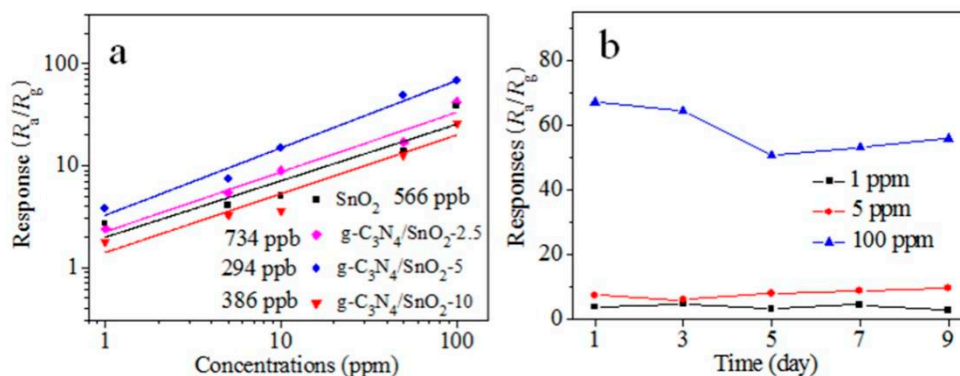


Figure 6. (a) Linear relationships between response and concentration of EA; (b) stability of material within nine days.

The effect of band structure changes on sensing performance has been analyzed by calculating the band gap energy of as-synthesized g-C₃N₄/SnO₂ from UV-vis results (Figure S4 and Figure 7a,c), and the linear extrapolation formula is referred to as our previous work [21]. The band gap energy is 2.92 and 2.86 eV for g-C₃N₄ and SnO₂, and 2.81 eV for g-C₃N₄/SnO₂-5 (Figure 7b,d). The results show that less energy can drive electrons to transfer from the valence to the conduction band, and the increased free electrons are helpful in improving the response to EA.

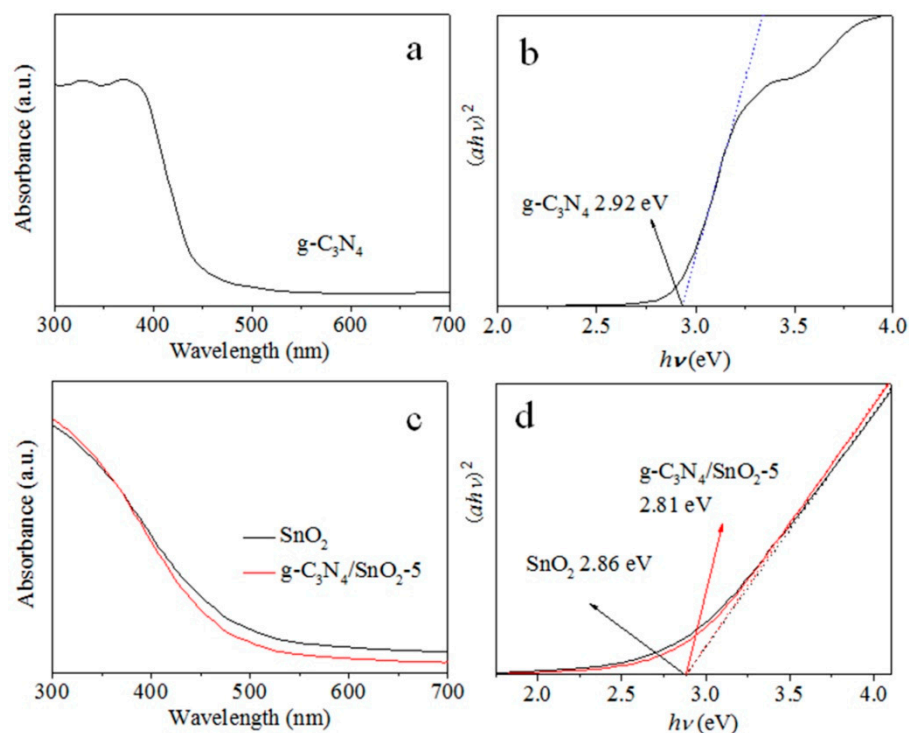


Figure 7. UV-vis DRS (a,c) and the band gap energy (b,d) of g-C₃N₄, SnO₂, and g-C₃N₄/SnO₂-5 materials (The dashed line is tangent extension line).

The sensing mechanism of n-type semiconductor materials conforms to the space charge layer model. When the sensor is moved from air to VOCs gases, the electron depletion layer formed on the surface of g-C₃N₄/SnO₂-5 changes, which can explain the gas sensitivity of g-C₃N₄/SnO₂-5 [30]. Therefore, the effect of different environmental conditions on the depletion layer width of g-C₃N₄/SnO₂-5 material is studied to explain the resistance variation of g-C₃N₄/SnO₂-5 sensor in air and EA. Figure 8 illustrates the formation of the electron depletion layer of the g-C₃N₄/SnO₂-5 sensor in air and EA gas. When g-C₃N₄/SnO₂-5 sensing material is in the air, oxygen molecules are adsorbed on the surface of g-C₃N₄/SnO₂-5 sensing material to form surface adsorbed oxygen (Figure 8), which will capture free electrons from the conduction band of g-C₃N₄/SnO₂-5 sensing material to form surface adsorbed oxygen ions (O^{α-}). There is a strong interaction between gas and surface [32]. A wide electron depletion layer is generated on the surface of g-C₃N₄/SnO₂-5, which causes a decrease in the carrier concentration and an increase in the resistance of the gas sensor. The formulas are as follows:



When the gas sensor is exposed to EA gas, it will react with chemisorbed oxygen (Figure 8). The reaction is represented as follows [23]:



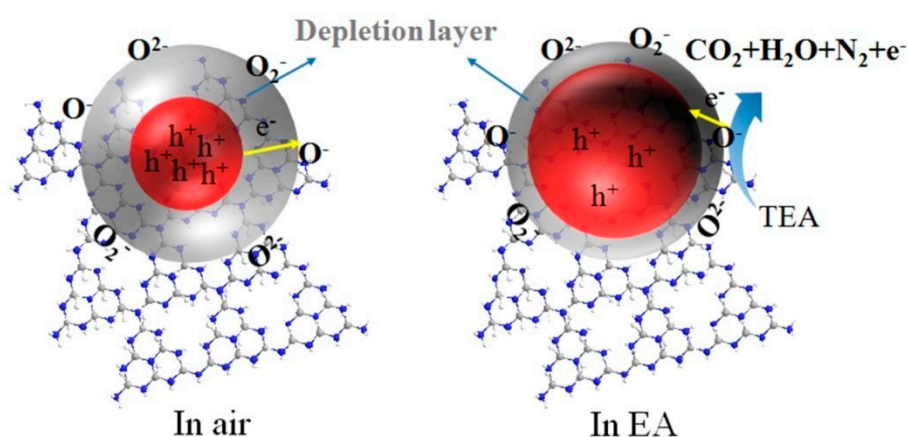


Figure 8. Schematic diagram of EA gas sensing mechanism of $g\text{-C}_3\text{N}_4/\text{SnO}_2$ material.

The captured electrons are released back into the conduction band of $g\text{-C}_3\text{N}_4/\text{SnO}_2$, and the thickness of the electron depletion layer of $g\text{-C}_3\text{N}_4/\text{SnO}_2$ material decreases, which results in an increase in the carrier concentration and decrease in the resistance of the $g\text{-C}_3\text{N}_4/\text{SnO}_2$ sensor. When $g\text{-C}_3\text{N}_4/\text{SnO}_2$ is exposed to air again, the chemisorption oxygen is produced, and the electron depletion layer becomes wide. Compared with pure SnO_2 , $g\text{-C}_3\text{N}_4/\text{SnO}_2$ exhibits superior gas sensitivity to EA. The possible reason is that $g\text{-C}_3\text{N}_4$ acts as a matrix to disperse SnO_2 nanoparticles and prevent aggregation of SnO_2 nanoparticles, which facilitates the adsorption and diffusion of oxygen molecules and EA molecules, and thus enhances the reaction of EA molecules with adsorbed oxygen ions, which are dependent on types of nano or microparticles and structure of sensing materials. In addition, the n-n heterojunction formed between the $g\text{-C}_3\text{N}_4$ and SnO_2 interface. When EA molecules cross through this interface, the electrical properties change at the heterojunction. The electrons transfer from the conduction band of $g\text{-C}_3\text{N}_4$ to the conduction band of SnO_2 , and the electrons and holes separate and finally a high potential barrier is created. The heterostructure between $g\text{-C}_3\text{N}_4$ and SnO_2 may inhibit the recombination of electron-hole pairs and promote the rapid transfer of electrons from EA to the surface of $g\text{-C}_3\text{N}_4/\text{SnO}_2$. As a result, the electrical conductivity of the heterojunction increases, which results in a high response.

To obtain theoretical evidence of energy band structure and conduction, model construction and calculation are conducted, and the details are put in Supporting Information according to similar methods [30,33,34]. Figure 9a–c show the structure models of $g\text{-C}_3\text{N}_4$, SnO_2 , and $g\text{-C}_3\text{N}_4/\text{SnO}_2$ materials, and the calculated energy band structures are shown in Figure 9d–f. The band gaps of the pure $g\text{-C}_3\text{N}_4$ and SnO_2 are marked in Figure 9d–f as 1.26 and 1.00 eV, respectively. It can also be seen that the top of the valence band (VBT) and the bottom of the conduction band (CBB) of $g\text{-C}_3\text{N}_4$ are centered at the Γ point and the A point, respectively (Figure 9d), while the VBT and CBB of SnO_2 are located at the S and X point (Figure 9e), which imply that $g\text{-C}_3\text{N}_4$ is an indirect band gap semiconductor and SnO_2 was a direct band gap semiconductor. [30] For the $g\text{-C}_3\text{N}_4/\text{SnO}_2$ material, it is clear that the energy band curves are more fine and close after the heterojunction is formed between SnO_2 and $g\text{-C}_3\text{N}_4$ (Figure 9f), leading to the electrons being reconstructed, and the band gap is closed to 0.0 eV (Figure 9f), indicating that the conductivity of $g\text{-C}_3\text{N}_4/\text{SnO}_2$ material has been improved significantly.

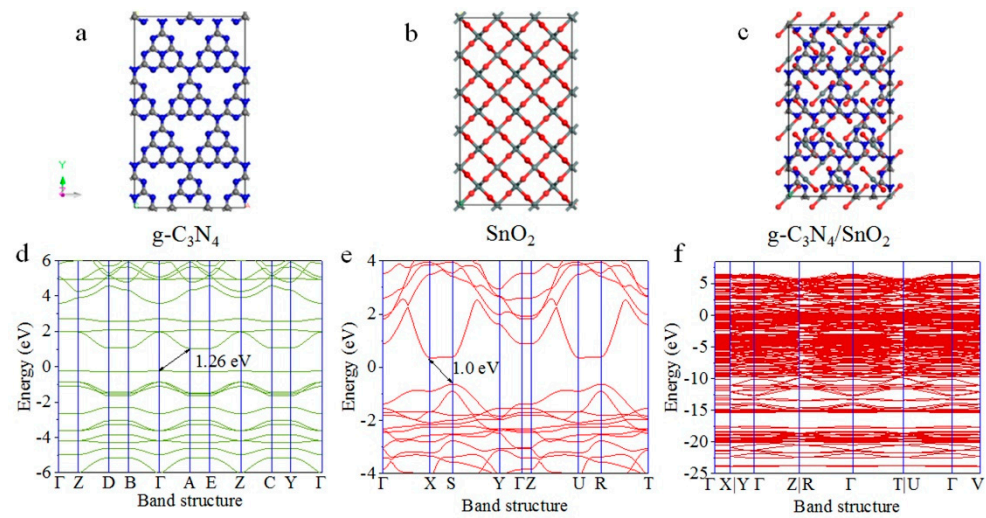


Figure 9. The crystal structure of (a) $g\text{-C}_3\text{N}_4$, (b) SnO_2 , and (c) $g\text{-C}_3\text{N}_4/\text{SnO}_2$. The calculated energy band structure of (d) $g\text{-C}_3\text{N}_4$, (e) SnO_2 , and (f) $g\text{-C}_3\text{N}_4/\text{SnO}_2$.

To further explore the change in conductivity of $g\text{-C}_3\text{N}_4/\text{SnO}_2$ material, the total density of states (TDOS) and partial density of states (PDOS) of $g\text{-C}_3\text{N}_4$, SnO_2 , and $g\text{-C}_3\text{N}_4/\text{SnO}_2$ were calculated, and the results are summarized in Figure 10. The main contribution of the valence band edge is C2p and N2p orbitals, and the conduction band edge is C2p and N2p orbitals for pure $g\text{-C}_3\text{N}_4$ (Figure 10a). The top of the SnO_2 valence band is Sn5s, 5p orbitals, and the bottom of the conduction band is Sn5p,4d and O2p orbitals (Figure 10b). For comparison, the DOS peaks shift to the left, and the peak at -15 eV increases. Notably, a new peak occurs near the Fermi level after SnO_2 modification (Figure 10c,d), showing that there is a strong orbital hybridization between SnO_2 and $g\text{-C}_3\text{N}_4$, and there is significant electron exchange between them.

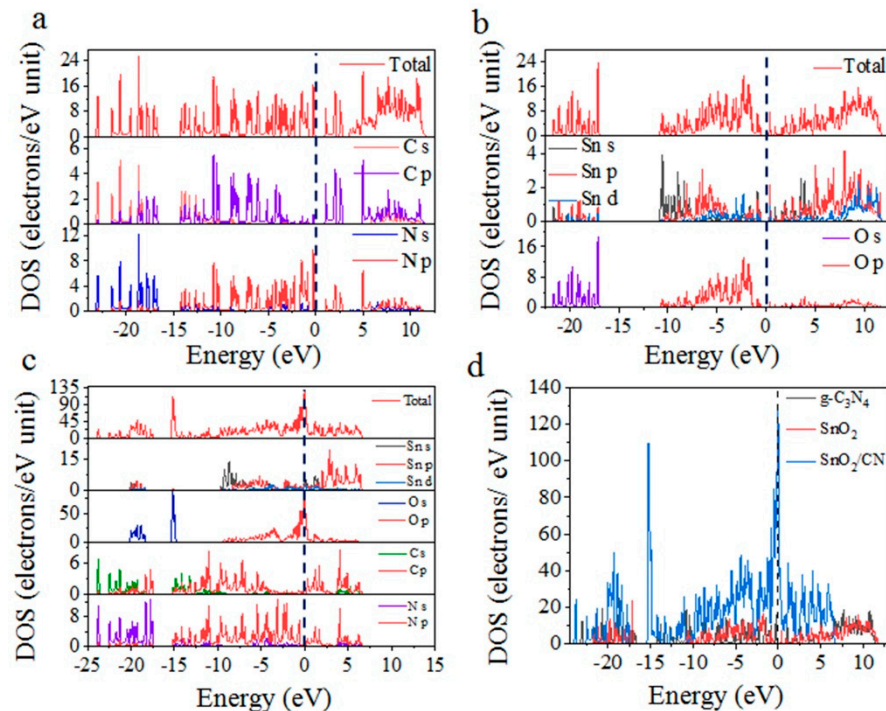


Figure 10. TDOS and PDOS of (a) $g\text{-C}_3\text{N}_4$, (b) SnO_2 , and (c) $g\text{-C}_3\text{N}_4/\text{SnO}_2$. (d) TDOS comparison of three materials.

4. Conclusions

g-C₃N₄/SnO₂ material was synthesized via a hydrothermal and pyrolysis route. Structural and morphology characterizations show that g-C₃N₄ acts as a matrix of SnO₂ to prevent the particles from agglomeration. As-obtained g-C₃N₄/SnO₂ exhibited higher response and selectivity to EA compared with pure SnO₂. The response to 100 ppm EA reaches ca. 68 at 240 °C, and it is superior to that of SnO₂. Enhanced sensing performance is attributed to the morphology, energy band, and structure of composites consisting of nanoparticles anchored on g-C₃N₄ layers, and the heterojunctions formed between SnO₂ and g-C₃N₄ interface resulting in fast electron transfer and increasing interstitial lattice defect sites, which can adsorb more O₂ molecules and provide more reactive oxygen species to react with EA molecules. This research provides a strategy to prepare new composite material for the effective detection of EA and other related organoamines released from tobacco and chemical industries.

Supplementary Materials: The following supporting information can be downloaded at: <https://www.mdpi.com/article/10.3390/chemosensors11050296/s1>, Figure S1: XRD patterns of g-C₃N₄; Figure S2: SEM images of as-synthesized materials (a) g-C₃N₄, (b) SnO₂, (c) g-C₃N₄/SnO₂-2.5, and (d) g-C₃N₄/SnO₂-10; Figure S3: XPS spectra of the full range spectrum of g-C₃N₄/SnO₂-5 material; Figure S4: (a) UV-Vis absorption spectra of g-C₃N₄, SnO₂, and g-C₃N₄/SnO₂ and (b) bandgap energy of g-C₃N₄, SnO₂, and g-C₃N₄/SnO₂.

Author Contributions: J.L.: Experimental work, data curation, and writing—original draft. K.X.: Data analysis and draft revision. Y.W.: Data analysis and draft revision. R.Z.: Supervision, conceptualization, and writing—review and editing. Y.S.: data curation and draft review and revision. J.D.: Experimental design, supervision, conceptualization, and writing—revision and editing. All authors have read and agreed to the published version of the manuscript.

Funding: This research is funded by the National Natural Science Foundation of China (No. 51572185), the Key R&D program of Shanxi Province (International Cooperation, No. 201903D421079), and the National Natural Science Foundation of Shanxi (No. 20210302123173).

Data Availability Statement: Not applicable.

Conflicts of Interest: The authors declare that they have no known competing financial interests.

References

1. Lv, D.; Lu, S.; Tan, X.; Shao, M.; Wang, L. Source profiles, emission factors and associated contributions to secondary pollution of volatile organic compounds (VOCs) emitted from a local petroleum refinery in Shandong. *Environ. Pollut.* **2021**, *3*, 116589. [[CrossRef](#)] [[PubMed](#)]
2. Hung, F.H.; Tsang, K.F.; Wu, C.K.; Liu, Y.; Wan, W.H. An Adaptive Indoor Air Quality Control Scheme for Minimizing Volatile Organic Compounds Density. *IEEE Access* **2020**, *8*, 22357–22365. [[CrossRef](#)]
3. Qin, J.; Wang, X.; Yang, Y.; Qin, Y.; Shi, S.; Xu, P.; Chen, R.; Zhou, X.; Tan, J.; Wang, X. Source apportionment of VOCs in a typical medium-sized city in North China Plain and implications on control policy. *J. Environ. Sci.* **2021**, *107*, 26–37. [[CrossRef](#)] [[PubMed](#)]
4. Yuan, Z.; Han, E.; Meng, F.; Zuo, K. Detection and identification of volatile organic compounds based on temperature-modulated ZnO sensors. *IEEE Trans. Instrum. Meas.* **2020**, *69*, 4533–4544. [[CrossRef](#)]
5. Wang, X.; Chen, F.; Yang, M.; Guo, L.; Xie, N.; Kou, X.; Song, Y.; Wang, Q.; Sun, Y.; Lu, G. Dispersed WO₃ nanoparticles with porous nanostructure for ultrafast toluene sensing. *Sens. Actuators B Chem.* **2019**, *289*, 195–206. [[CrossRef](#)]
6. Meng, F.; Zheng, H.; Chang, Y.; Zhao, Y.; Li, M.; Wang, C.; Sun, Y.; Liu, J. One-step synthesis of Au/SnO₂/RGO nanocomposites and their VOC sensing properties. *IEEE Trans. Nanotechnol.* **2018**, *17*, 212–219. [[CrossRef](#)]
7. Zhang, P.; Zhang, L.; Xu, H.; Xing, Y.; Chen, J.; Bie, L. Ultrathin CeO₂ nanosheets as bifunctional sensing materials for humidity and formaldehyde detection. *Rare Met.* **2021**, *40*, 1614–1621. [[CrossRef](#)]
8. Bhat, P.; Kumar, S.N. Evaluation of IDE-based flexible thin film ZnO sensor for VOC sensing in a custom designed gas chamber at room temperature. *J. Mater. Sci.-Mater. Electron.* **2022**, *33*, 1529–1541. [[CrossRef](#)]
9. Zhang, H.; Shi, W.; Gao, N.; Zhao, R.; Ahmed, M.; Li, J.; Du, J.; Asefa, T. Highly sensitive and selective gas-phase ethanolamine sensor by doping sulfur into nanostructured ZnO. *Sens. Actuators B Chem.* **2019**, *296*, 126633. [[CrossRef](#)]
10. Zhang, K.; Xie, K.; Ahmed, M.; Chai, Z.; Zhao, R.; Li, J.; Du, J. Cr-doped SnO₂ microrod adhering nanoparticles for enhanced triethylamine sensing performance. *Mater. Lett.* **2022**, *312*, 131684. [[CrossRef](#)]
11. Shang, Y.; Shi, W.; Zhao, R.; Ahmed, M.; Li, J.; Du, J. Simple self-assembly of 3D laminated CuO/SnO₂ hybrid for the detection of triethylamine. *Chin. Chem. Lett.* **2020**, *31*, 2055–2058. [[CrossRef](#)]

12. Du, J.; Xie, Y.; Yao, H.; Zhao, R.; Li, J. Size-dependent gas sensing and selectivity of SnO₂ quantum dots toward volatile compounds. *Appl. Surf. Sci.* **2015**, *346*, 256–262. [[CrossRef](#)]
13. Acharyya, S.; Jana, B.; Nag, S.; Saha, G.; Guha, P.K. Single resistive sensor for selective detection of multiple VOCs employing SnO₂ hollow spheres and machine learning algorithm: A proof of concept. *Sens. Actuators B Chem.* **2020**, *321*, 128484. [[CrossRef](#)]
14. Meng, F.; Ji, H.; Yuan, Z.; Chen, Y.; Gao, H. Dynamic Measurement and Recognition Methods of SnO₂ Sensor to VOCs under Zigzag-rectangular Wave Temperature Modulation. *IEEE Sens. J.* **2021**, *21*, 10915–10922. [[CrossRef](#)]
15. Du, J.; He, S.; Zhao, R.; Chen, S.; Guo, T.; Wang, H. Facile self-assembly of SnO₂ nanospheres for volatile amines gas sensing. *Mater. Lett.* **2017**, *186*, 318–321. [[CrossRef](#)]
16. Zhang, R.; Xu, Z.; Zhou, T.; Fei, T.; Wang, R.; Zhang, T. Improvement of gas sensing performance for tin dioxide sensor through construction of nanostructures. *J. Colloid Interface Sci.* **2019**, *557*, 673–682. [[CrossRef](#)]
17. Ma, X.; Gao, R.; Zhang, T.; Sun, X.; Li, T.; Gao, S.; Zhang, X.; Xu, Y.; Cheng, X.; Huo, L. Mesoporous SnO₂ nanospheres sensor for fast detection of HCHO and its application in safety detection of aquatic products. *Sens. Actuators B Chem.* **2022**, *374*, 132844. [[CrossRef](#)]
18. Din, S.U.; Ul Haq, M.; Sajid, M.; Khatoon, R.; Chen, X.; Li, L.; Zhang, M.; Zhu, L. Development of high-performance sensor based on NiO/SnO₂ heterostructures to study sensing properties towards various reducing gases. *Nanotechnology* **2020**, *31*, 395502. [[CrossRef](#)]
19. Dai, H.; Ding, J.; Chen, H.; Fu, H. Improvement of ethanolamine sensing performance based on Au-modified ZnO rod-like nanoflowers. *Mater. Lett.* **2023**, *340*, 134183. [[CrossRef](#)]
20. Zou, Z.; Zhao, Z.; Zhang, Z.; Tian, W.; Yang, C.; Jin, X.; Zhang, K. Room-temperature optoelectronic gas sensor based on core-shell-g-C₃N₄@WO₃ heterocomposites for efficient ammonia detection. *Anal. Chem.* **2023**, *95*, 2110–2118. [[CrossRef](#)]
21. Bai, K.; Cui, Z.; Li, E.; Ding, Y.; Zheng, J.; Liu, C.; Zheng, Y. Adsorption of gas molecules on group III atoms adsorbed g-C₃N₄: A first-principles study. *Vacuum* **2020**, *175*, 109293. [[CrossRef](#)]
22. Chen, M.; Guo, C.; Hou, S.; Lv, J.; Xu, J. A novel Z-scheme AgBr/P-g-C₃N₄ heterojunction photocatalyst: Excellent photocatalytic performance and photocatalytic mechanism for ephedrine degradation. *Appl. Catal. B-Environ.* **2020**, *266*, 118614. [[CrossRef](#)]
23. Li, L.; Huang, Z.; Li, Z.; Li, H.; Wang, A. Defect-rich porous g-C₃N₄ nanosheets photocatalyst with enhanced photocatalytic activity. *J. Mater. Sci.-Mater. Electron.* **2021**, *32*, 6465–6474. [[CrossRef](#)]
24. Liu, P.; Zhang, Z.; Hao, R.; Huang, Y.; Liu, K. Ultra-highly stable zinc metal anode via 3D-printed g-C₃N₄ modulating interface for long life energy storage systems. *Chem. Eng. J.* **2020**, *403*, 126425. [[CrossRef](#)]
25. Lin, Z. Preparation of ZnO/layered g-C₃N₄ and their n-butanol gas sensing properties. *Mater. Sci.* **2020**, *10*, 278–286.
26. Yuan, B.; Wang, Y.; Elnaggar, A.Y.; Azab, I.H.E.; Huang, M.; Mahmoud, M.H.H.; El-Bahy, S.M.; Guo, M. Physical vapor deposition of graphitic carbon nitride (g-C₃N₄) films on biomass substrate: Optoelectronic performance evaluation and life cycle assessment. *Adv. Compos. Hybrid. Mater.* **2022**, *5*, 813–822. [[CrossRef](#)]
27. Cao, J.; Qin, C.; Wang, Y.; Zhang, B.; Gong, Y.; Zhang, H.; Sun, G.; Bala, H.; Zhang, Z. Calcination method synthesis of SnO₂/g-C₃N₄ composites for a high-performance ethanol gas sensing application. *Nanomaterials* **2017**, *7*, 98. [[CrossRef](#)]
28. Wang, H.; Bai, J.; Dai, M.; Liu, K.; Liu, Y.; Zhou, L.; Liu, F.; Li, F.; Gao, Y.; Yan, X.; et al. Visible light activated excellent NO₂ sensing based on 2D/2D ZnO/g-C₃N₄ heterojunction composites. *Sens. Actuators B Chem.* **2020**, *304*, 127287. [[CrossRef](#)]
29. Niu, J.; Wang, L.; Xu, J.; Jin, H.; Hong, B.; Jin, D.; Peng, X.; Ge, H.; Wang, X. Mesoporous Co₃O₄ nanowires decorated with g-C₃N₄ nanosheets for high performance toluene gas sensors based on p-n heterojunction. *Mater. Chem. Phys.* **2023**, *293*, 126980. [[CrossRef](#)]
30. Xie, K.; Wang, Y.; Zhang, K.; Zhao, R.; Chai, Z.; Du, J.; Li, J. Controllable band structure of ZnO/g-C₃N₄ aggregation to enhance gas sensing for the dimethylamine detection. *Sens. Actuators Rep.* **2022**, *4*, 100084. [[CrossRef](#)]
31. Ni, J.; Wang, Y.; Liang, H.; Kang, Y.; Liu, B.; Zhao, R.; Wang, Y.; Shuai, X.; Shang, Y.; Guo, T.; et al. Facile template-free preparation of hierarchically porous graphitic carbon nitrides as high-performance photocatalyst for degradation of methyl violet dye. *ChemistrySelect* **2021**, *6*, 7130–7135. [[CrossRef](#)]
32. Stefan, K.; Chris, B. Atomistic Descriptions of gas–surface interactions on tin dioxide. *Chemosensors* **2021**, *9*, 270.
33. Wang, V.; Xu, N.; Liu, J.C. VASPKIT: A user-friendly interface facilitating high-throughput computing and analysis using VASP code. *Computer Phys. Commun.* **2021**, *267*, 108033. [[CrossRef](#)]
34. Liangruksa, M.; Sukpoonprom, P.; Junkaew, A.; Photaram, W.; Siriwong, C. Gas sensing properties of palladium-modified zinc oxide nanofilms: A DFT study. *Appl. Surf. Sci.* **2021**, *544*, 148868. [[CrossRef](#)]

Disclaimer/Publisher’s Note: The statements, opinions and data contained in all publications are solely those of the individual author(s) and contributor(s) and not of MDPI and/or the editor(s). MDPI and/or the editor(s) disclaim responsibility for any injury to people or property resulting from any ideas, methods, instructions or products referred to in the content.